

1 **Supplemental Material for *Nontrivial scaling in supply***
2 ***limited Aeolian sand transport***

3 **Sandesh Kamath¹, Yaping Shao¹, Eric J. R. Parteli²**

4 ¹Institute of Geophysics and Meteorology, University of Cologne, Germany

5 ²Faculty of Physics, University of Duisburg-Essen, Germany

Corresponding author: Sandesh Kamath, skamath@uni-koeln.de

6 Abstract

7 In this Supplemental Material, we briefly review the features of the Discrete-Element-
 8 Method referred to in the main document, including the complete set of the equations
 9 of motion, the details of the numerical integration of these equations, and the models of
 10 particle-particle interactions adopted in the simulations of Aeolian sand transport. Further-
 11 more, we present the results of our numerical simulations performed to verify our model,
 12 the vertical profiles of the wind velocity and grain-borne shear stress during steady-state
 13 transport, and the behavior of the transport layer thickness as a function of the thickness
 14 of mobile sand layer, as mentioned in the main document.

15 1 Discrete-Element-Method

16
 17 In the Discrete-Element-Method, the equations of motion are solved for every particle in
 18 the system under consideration of the main forces acting on them. These forces are, in
 19 the process of non-suspended Aeolian transport of cohesionless particles, the drag force, the
 20 inter-particle contact forces and the gravitational force.

21 1.1 Equations of motion and contact force model for the sand particles

22 The equation of translational motion for a particle of mass m_i at position \mathbf{r}_i reads,

$$23 \quad m_i \ddot{\mathbf{r}}_i = \mathbf{F}_i^d + m_i \mathbf{g} + \sum_{\substack{1 \leq j \leq N_p \\ j \neq i}} \mathbf{F}_{ij}^c \quad (1)$$

24 where \mathbf{F}_i^d is the drag force on particle i , computed with the model described in the main
 25 document, \mathbf{g} is gravity, N_p is the number of particles in the system, j denotes the index of
 26 a neighbouring particle that is in contact with particle i , and \mathbf{F}_{ij}^c denotes the contact force
 27 exerted by particle j on i (with $\mathbf{F}_{ij}^c = -\mathbf{F}_{ji}^c$).

28 Contact between particles j and i occurs with their center-to-center distance is smaller than
 29 the sum of their radii, i.e., the contact force acts only if the particles overlap. To model the
 30 contact force, the following equation is used to define the overlap,

$$31 \quad \delta_{ij,n} = \min \left\{ 0, \frac{1}{2} [d_i + d_j] - (\mathbf{r}_i - \mathbf{r}_j) \cdot \mathbf{e}_{ij,n} \right\} \quad (2)$$

32 where d_i and d_j are the diameters of particles i and j , respectively, $\mathbf{r}_{ij} = \mathbf{r}_i - \mathbf{r}_j$, with \mathbf{r}_j
 33 standing for the position of particle j , and $\mathbf{e}_{ij,n} = \mathbf{r}_{ij}/r_{ij}$ denotes the normal unit vector
 34 pointing from the center of particle j to the center of particle i , with $r_{ij} = |\mathbf{r}_{ij}|$.

35 There are various contact force models for application in DEM simulations, and the mod-
 36 elling of these forces is still an active matter of research (Cundall & Strack, 1979; Schäfer et
 37 al., 1996; Brilliantov et al., 1996; Silbert et al., 2001; Di Renzo & Di Maio, 2004; Pöschel &
 38 Schwager, 2005; Kruggel-Emden et al., 2007; Luding, 2008; Machado et al., 2012; Parteli et
 39 al., 2014; Fan et al., 2017; Schmidt et al., 2020; Santos et al., 2020). In our simulations, we
 40 adopt the linear spring-dashpot model, because this model has been employed in previous
 41 simulations of wind-blown sand that reproduced the scaling laws associated with Aeolian
 42 transport over fully erodible beds (Carneiro et al., 2011, 2013; Durán et al., 2012; Comola
 43 et al., 2019).

44 Specifically, \mathbf{F}_{ij}^c can be described as the sum of a normal component, $\mathbf{F}_{ij,n}^c$, and a tangential
 45 component, $\mathbf{F}_{ij,t}^c$. Each of these components encodes an elastic term and a dissipative term,
 46 while the magnitude of the tangential force is bounded by the Coulomb friction criterion.
 47 The equations for $\mathbf{F}_{ij,n}^c$ and $\mathbf{F}_{ij,t}^c$ read (Cundall & Strack, 1979; Silbert et al., 2001; Santos

et al., 2020)

$$\mathbf{F}_{ij,n}^c = k_n \delta_{ij,n} \mathbf{e}_{ij,n} - \gamma_n m_{\text{eff}} \mathbf{v}_{ij,n} \quad (3)$$

$$\mathbf{F}_{ij,t}^c = -\min\{\mu_s |\mathbf{F}_{ij,n}^c|, k_t \xi_{ij,t} + \gamma_t m_{\text{eff}} |\mathbf{v}_{ij,t}|\} \frac{\mathbf{v}_{ij,t}}{|\mathbf{v}_{ij,t}|} \quad (4)$$

where $m_{\text{eff}} = m_i m_j / (m_i + m_j)$, with m_i and m_j denoting the masses of particles i and j , respectively, k_n , k_t , γ_n , γ_t and μ_s are model parameters, discussed in Section 1.3 below, while the relative normal velocity $\mathbf{v}_{ij,n}$ and the relative tangential velocity $\mathbf{v}_{ij,t}$ between particles i and j are computed via

$$\mathbf{v}_{ij,n} = (\mathbf{v}_{ij} \cdot \mathbf{e}_{ij,n}) \mathbf{e}_{ij,n} \quad (5)$$

$$\mathbf{v}_{ij,t} = \mathbf{v}_{ij} - \mathbf{v}_{ij,n} - \frac{1}{2}(\boldsymbol{\omega}_i + \boldsymbol{\omega}_j) \times (\mathbf{r}_i - \mathbf{r}_j) \quad (6)$$

with $\mathbf{v}_{ij} = \mathbf{v}_i - \mathbf{v}_j$ denoting the difference between the velocities of particles i and j (\mathbf{v}_i and \mathbf{v}_j , respectively), and $\boldsymbol{\omega}_i$ and $\boldsymbol{\omega}_j$ standing for their respective rotational velocities. Moreover, in Eq. (4), $\xi_{ij,t}$ is the tangential displacement accumulated as the particles are in contact. The displacement is set as zero at initiation of the contact and is computed in the reference frame of the rotating particle pair to compensate for the effect of rigid body rotations, as described in detail in previous work (Silbert et al., 2001; Santos et al., 2020).

The equation of rotational motion for particle i reads

$$I_i \boldsymbol{\omega}_i = \sum_{\substack{1 \leq j \leq N_p \\ j \neq i}} \mathbf{M}_{ij} \quad (7)$$

with $I_i = m_i d_i^2 / 10$ and $\boldsymbol{\omega}_i$ denoting the moment of inertia and the angular velocity of particle i , respectively, and \mathbf{M}_{ij} corresponding to the torque on particle i associated with $\mathbf{F}_{ij,t}^c$.

1.2 Contact forces between mobile and rigid particles (non-erodible elements)

The contact forces between mobile sand particles and the rigid particles constituting the roughness elements of the bed are computed using the same model as in the previous section, but considering that the rigid particles have an infinite mass (Verbücheln et al., 2015). Specifically, the normal and tangential components of the contact force from a rigid particle j on a mobile particle i are computed with Eqs. (3) and (4), respectively, by setting $m_{\text{eff}} = m_i$. Furthermore, contact forces between rigid particles are not considered.

1.3 Model parameters

Table 1 displays the values of the parameters in Eqs. (3) and (4), i.e., the elastic constants k_n and k_t , the damping coefficients γ_n and γ_t , and the Coulomb friction coefficient, μ_s . The elastic and damping constants are taken from previous models for Aeolian sand transport over fully erodible beds (Carneiro et al., 2011, 2013; Comola et al., 2019). In particular, the elastic constant for normal contact, k_n , is estimated using $k_n = \pi d_m Y / 4$, where $d_m = 200 \mu\text{m}$ is the mean particle size adopted in our simulations, while $Y = 1 \text{ MPa}$ is the Young's modulus adopted in previous work (Carneiro et al., 2011; Comola et al., 2019) and in our computations. Furthermore, for the elastic constant for tangential constant, we use $k_t = k_n / 3$, while the friction coefficient is consistent with values adopted previously (Comola et al., 2019).

Table 1: Parameters of the Discrete-Element-Method.

parameter	symbol	value
elastic constant for normal contact	k_n	157
elastic constant for tangential contact	k_t	52
viscoelastic damping constant for normal contact	γ_n	0.2
viscoelastic damping constant for tangential contact	γ_t	0.2
Coulomb coefficient of friction	μ_s	0.3
particle diameter	d_i	[160, 240] μm
particle density	ρ_p	2650 kg m^{-3}

1.4 Numerical implementation and particle-wind coupling

To solve the equations of motion of the granular phase, we employ LAMMPS (Large-scale Atomic/Molecular Massively Parallel Simulator), which is an open source DEM solver based on MPI implementation (Plimpton, 1995). Furthermore, we have extended this solver to incorporate the hydrodynamic description of the turbulent wind flow over the granular surface, developed in previous work (Carneiro et al., 2011; Durán et al., 2012) and briefly reviewed in the main document. To this end, we have included new modules (LAMMPS “fixes”) into the granular package of the DEM solver, to set the initial (logarithmic) vertical profile of the mean horizontal wind speed, to compute the drag force, and to update this drag force and the wind profile owing to the process of momentum exchange between the particles and the wind. These modules are available from the corresponding author upon request.

2 Validation of our simulations over fully erodible beds

To verify our numerical simulations, we compare our numerical predictions for the height-integrated mass flux (Q) of wind-blown particles over a fully erodible bed with corresponding wind-tunnel observations of this flux as a function of the wind shear velocity, u_* . We compute Q using the following equation,

$$Q = \frac{\sum_i^N m_i v_i^x}{A} \quad (8)$$

where N is the number of particles in the system, m_i and v_i^x denote the mass and horizontal speed of the i -th particle, respectively, and $A = L_x \cdot L_y$ is the horizontal area of the simulation domain. To measure this flux, we start the wind-blown transport process as described in the main document and wait until this transport achieves steady-state. The typical (physical) time separating the begin of wind-blown transport from the steady-state is about 2-3 seconds and independent of u_* (Carneiro et al., 2011; Durán et al., 2012; Pähz et al., 2014; Comola et al., 2019). All results reported in the present work refer to the characteristics of steady-state (saturated) wind-blown transport, and denote mean quantities obtained from averaging over about 5-10 seconds during steady-state transport.

Furthermore, by suitably normalizing the steady-state flux Q , we obtain the following non-dimensional quantity,

$$\hat{Q} = \frac{Q}{\rho_p \sqrt{(s-1)gd_m^3}}, \quad \text{with } s = \frac{\rho_p}{\rho_f}, \quad (9)$$

which we plot in Fig. S1 as a function of the Shields number,

$$\Theta = \frac{u_*^2 \rho_f}{(\rho_p - \rho_f)gd_m} \quad (10)$$

121 where $\rho_p = 2650 \text{ kg/m}^3$ and $\rho_f = 1.225 \text{ kg/m}^3$ denote the densities of the particles and the
 122 air, respectively, while $d_m = 200 \mu\text{m}$ is the mean particle diameter and $g = 9.81 \text{ m/s}^2$ is
 gravity.

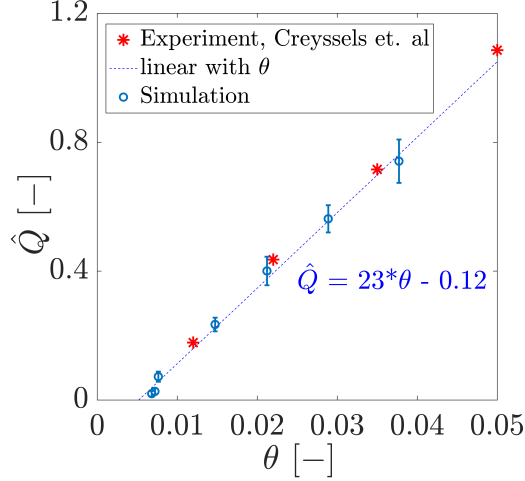


Figure S1: Normalized steady-state flux \hat{Q} as a function of the Shields number Θ , considering a fully erodible bed ($h_{\text{mob}} \approx 15 d_m$).

123

124 We see in Fig. S1 that our numerical predictions for $\hat{Q}(\Theta)$ (circles) agree quantitatively well
 125 with observations from wind-tunnel experiments (Creyssels et al., 2009), denoted by the
 126 stars. The best fit to our simulation results using $\hat{Q} = a\Theta + b$ yields $a \approx 23$ and $b \approx 0.12$
 127 (dashed line in Fig. S1), from which obtain the minimal threshold $\Theta_t \approx 0.0064$ below which
 128 no transport occurs ($\hat{Q} = 0$). From Eq. (10), this value of Θ_t leads to the minimal threshold
 129 wind shear velocity for sustained transport, $u_{*t} \approx 0.165 \text{ m/s}$.

130 We note that the value of u_{*t} predicted from our simulations is consistent with the prediction
 131 that u_{*t} is about 80% of the minimal threshold wind shear velocity u_{*ft} required to initiate
 132 transport,

$$133 \quad u_{*ft} = A_{ft} \sqrt{\frac{\rho_p - \rho_f}{\rho_f} g d_m}, \quad (11)$$

134 with $A_{ft} \approx 0.1$ (Bagnold, 1941; Shao & Lu, 2000). Indeed, by applying the mean particle
 135 size $d_m = 200 \mu\text{m}$ of our simulations in Eq. (11), we obtain $u_{*ft} \approx 0.206 \text{ m/s}$, i.e., our model
 136 is consistent with the relation $u_{*t} \approx 0.8 u_{*ft}$ predicted for wind-blown transport.

137 3 The modified wind profiles for varying h_{mob}

138 The initial vertical profile of the horizontal downstream wind velocity u_x is logarithmic and
 139 follows Eq. (3) of the main document. However, this wind velocity profile is updated every
 140 time-step, since the acceleration of the grains extracts momentum from the air thus creating
 141 a negative feedback on the wind. The modification of the wind velocity profile is computed
 142 using Eqs. (4) and (5) in the main document. The vertical profiles of the modified wind
 143 velocity u_x and the grain-borne shear stress τ_p are shown for different values of the mobile
 144 layer thickness h_{mob} in Fig. S2.

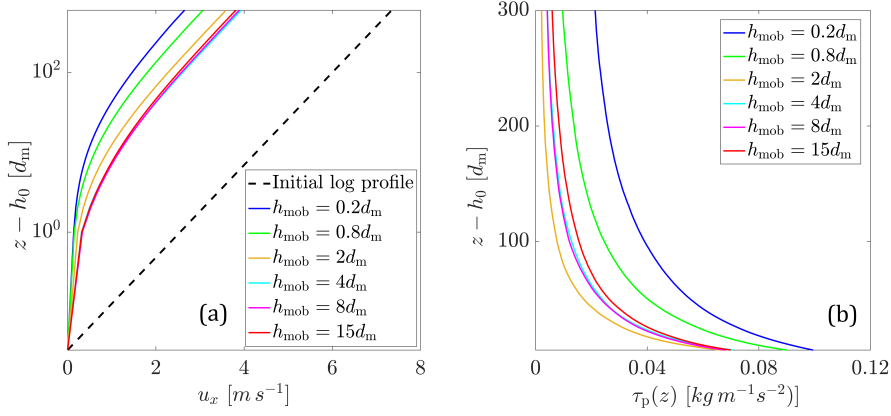


Figure S2: (a) The modified wind profiles for different values of h_{mob} alongside the initial logarithmic profile; (b) grain-borne shear stress profile as a function of the height above the bed for different h_{mob} . The results were obtained with $u_* = 0.30$ m/s.

4 Transport layer thickness as a function of h_{mob}

As explained in the main document, the transport layer expands gradually as the soil erodibility conditions change from fully erodible to rigid. To quantify this process, we compute the characteristic length-scale l_ν associated with the nearly exponential decay of the particle concentration $\nu(z)$ with the height z above the ground, i.e.,

$$\nu(z) = \nu_0 \exp(-z/l_\nu) \quad (12)$$

where ν_0 is the particle concentration extrapolated to the bed ($z = 0$). Fig. S3 shows the behavior of l_ν as a function of the thickness of mobile sand layer on the ground, h_{mob} . We

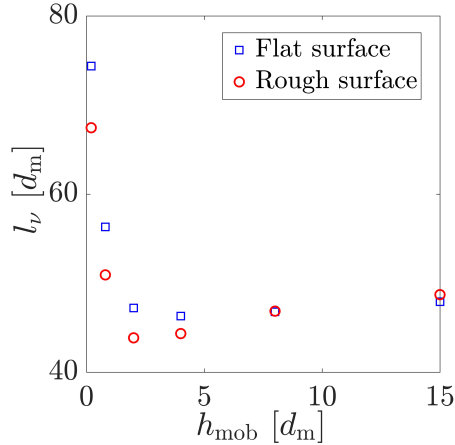


Figure S3: Thickness l_ν of the transport layer as a function of the thickness h_{mob} of the mobile sediment layer covering the non-erodible surface, which consists of a flat horizontal surface (blue symbols) and a sheet of immobile particles (red symbols). The results were obtained with $u_* = 0.30$ m/s.

153 see that, when the rigid ground is flat, l_ν decreases monotonically as h_{mob} increases toward
 154 $15 d_m$ (the fully erodible bed scenario). However, when the rigid surface is armoured with
 155 non-erodible elements (which in our simulations have the same size as the mobile particles),
 156 a minimum in l_ν is observed near $h_{\text{mob}} = 2 d_m$. This minimum can be explained by the
 157 prevailing occurrence of backward ejecta in the range $h_{\text{mob}} \lesssim 2 d_m$ (as described in the main
 158 document), which leads to lower values of l_ν in this range when non-erodible particles cover
 159 the ground, compared to the flat ground scenario. As h_{mob} increases toward $15 d_m$, the
 160 effect of the immobile particles on the Aeolian transport thickness becomes negligible, and
 161 l_ν approaches asymptotically the value corresponding to the fully erodible bed as shown in
 162 Fig. S3.

163 Acknowledgments

164 The data for validation with experiments in Fig. S1 is available from (Creyssels et al., 2009),
 165 and the rest is made available online (<https://doi.org/10.6084/m9.figshare.14473848.v1>).
 166 We thank the German Research Foundation (DFG) for funding through the Heisenberg
 167 Programme and the grant - 348617785.

168 References

- 169 Bagnold, R. A. (1941). *The physics of blown sand and desert dunes*. Methuen, London.
- 170 Brilliantov, N. V., Spahn, F., Hertzsch, J.-M., & Pöschel, T. (1996). Model for collisions
 171 in granular gases. *Physical review E*, *53*(5), 5382. doi: [https://doi.org/10.1103/](https://doi.org/10.1103/PhysRevE.53.5382)
 172 [PhysRevE.53.5382](https://doi.org/10.1103/PhysRevE.53.5382)
- 173 Carneiro, M. V., Araújo, N. A. M., Pähz, T., & Herrmann, H. J. (2013). Midair collisions
 174 enhance saltation. *Physical review letters*, *111*(5), 058001. doi: [https://doi.org/](https://doi.org/10.1103/PhysRevLett.111.058001)
 175 [10.1103/PhysRevLett.111.058001](https://doi.org/10.1103/PhysRevLett.111.058001)
- 176 Carneiro, M. V., Pähz, T., & Herrmann, H. J. (2011). Jump at the onset of saltation.
 177 *Physical Review Letters*, *107*(9), 098001. doi: [https://doi.org/10.1103/PhysRevLett](https://doi.org/10.1103/PhysRevLett.107.098001)
 178 [.107.098001](https://doi.org/10.1103/PhysRevLett.107.098001)
- 179 Comola, F., Gaume, J., Kok, J., & Lehning, M. (2019). Cohesion-induced enhancement
 180 of aeolian saltation. *Geophysical Research Letters*, *46*(10), 5566–5574. doi: [https://](https://doi.org/10.1029/2019GL082195)
 181 doi.org/10.1029/2019GL082195
- 182 Creyssels, M., Dupont, P., El Moctar, A. O., Valance, A., Cantat, I., Jenkins, J. T., ...
 183 Rasmussen, K. R. (2009). Saltating particles in a turbulent boundary layer: ex-
 184 periment and theory. *J. Fluid Mechanics*, *625*, 47. doi: [https://doi.org/10.1017/](https://doi.org/10.1017/S0022112008005491)
 185 [S0022112008005491](https://doi.org/10.1017/S0022112008005491)
- 186 Cundall, P. A., & Strack, O. D. (1979). A discrete numerical model for granular assemblies.
 187 *geotechnique*, *29*(1), 47–65. doi: <https://doi.org/10.1680/geot.1979.29.1.47>
- 188 Di Renzo, A., & Di Maio, F. P. (2004). Comparison of contact-force models for the simulation
 189 of collisions in dem-based granular flow codes. *Chemical Engineering Science*, *59*(3),
 190 525–541. doi: <https://doi.org/10.1016/j.ces.2003.09.037>
- 191 Durán, O., Andreotti, B., & Claudin, P. (2012). Numerical simulation of turbulent sediment
 192 transport, from bed load to saltation. *Physics of Fluids*, *24*(10), 103306. doi: [https://](https://doi.org/10.1063/1.4757662)
 193 doi.org/10.1063/1.4757662
- 194 Fan, F., Parteli, E. J. R., & Pöschel, T. (2017). Origin of granular capillarity revealed
 195 by particle-based simulations. *Phys. Rev. Lett.*, *118*, 218001. doi: [https://doi.org/](https://doi.org/10.1103/PhysRevLett.118.218001)
 196 [10.1103/PhysRevLett.118.218001](https://doi.org/10.1103/PhysRevLett.118.218001)
- 197 Kruggel-Emden, H., Simsek, E., Rickelt, S., Wirtz, S., & Scherer, V. (2007). Review and
 198 extension of normal force models for the discrete element method. *Powder Technol.*,
 199 *171*, 157–173. doi: <https://doi.org/10.1016/j.powtec.2006.10.004>
- 200 Luding, S. (2008). Cohesive, frictional powders: contact models for tension. *Granular*
 201 *matter*, *10*(4), 235. doi: <https://doi.org/10.1007/s10035-008-0099-x>
- 202 Machado, M., Moreira, P., Flores, P., & Lankarani, H. M. (2012). Compliant contact force
 203 models in multibody dynamics: Evolution of the hertz contact theory. *Mechanism and*

- 204 *Machine Theory*, 53, 99-121. doi: <https://doi.org/10.1016/j.mechmachtheory.2012.02>
205 .010
- 206 Pähz, T., Parteli, E. J. R., Kok, J. F., & Herrmann, H. J. (2014). Analytical model
207 for flux saturation in sediment transport. *Physical Review E*, 89(5), 052213. doi:
208 <https://doi.org/10.1103/PhysRevE.89.052213>
- 209 Parteli, E. J. R., Schmidt, J., Blümel, C., Wirth, K.-E., Peukert, W., & Pöschel, T. (2014).
210 Attractive particle interaction forces and packing density of fine glass powders. *Sci.*
211 *Rep.*, 4, 6227. doi: <https://doi.org/10.1038/srep06227>
- 212 Plimpton, S. (1995). Fast parallel algorithms for short-range molecular dynamics. *Journal of*
213 *computational physics*, 117(1), 1–19. (Website of the DEM solver LAMMPS: [https://](https://lammms.sandia.gov/)
214 lammms.sandia.gov/) doi: <https://doi.org/10.1006/jcph.1995.1039>
- 215 Pöschel, T., & Schwager, T. (2005). *Computational granular dynamics*. Springer Berlin
216 Heidelberg. doi: <https://doi.org/10.1007/3-540-27720-X>
- 217 Santos, A. P., Bolintineanu, D. S., Grest, G. S., Lechman, J. B., Plimpton, S. J., Srivastava,
218 I., & Silbert, L. E. (2020). Granular packings with sliding, rolling, and twisting friction.
219 *Phys. Rev. E*, 102, 032903. doi: <https://doi.org/10.1103/PhysRevE.102.032903>
- 220 Schäfer, J., Dippel, S., & Wolf, D. E. (1996). Force Schemes in Simulations of Granular
221 Materials. *J. Phys. I France*, 6, 5-20. doi: <https://doi.org/10.1051/jp1:1996129>
- 222 Schmidt, J., Parteli, E. J., Uhlmann, N., Wörlein, N., Wirth, K.-E., Pöschel, T., & Peukert,
223 W. (2020). Packings of micron-sized spherical particles: Insights from bulk density de-
224 termination, x-ray microtomography and discrete element simulations. *Advanced Pow-*
225 *der Technology*, 31(6), 2293-2304. doi: <https://doi.org/10.1016/j.apr.2020.03.018>
- 226 Shao, Y., & Lu, H. (2000). A simple expression for wind erosion threshold friction velocity.
227 *Journal of Geophysical Research: Atmospheres*, 105(D17), 22437-22443. doi: [https://](https://doi.org/10.1029/2000JD900304)
228 doi.org/10.1029/2000JD900304
- 229 Silbert, L. E., Ertas, D., Grest, G. S., Halsey, T. C., Levine, D., & Plimpton, S. J. (2001).
230 Granular flow down an inclined plane: Bagnold scaling and rheology. *Physical Review*
231 *E*, 64(5), 051302. doi: <https://doi.org/10.1103/PhysRevE.64.051302>
- 232 Verbücheln, F., Parteli, E. J. R., & Pöschel, T. (2015). Helical inner-wall texture prevents
233 jamming in granular pipe flows. *Soft Matter*, 11(21), 4295–4305. doi: [https://doi.org/](https://doi.org/10.1039/c5sm00760g)
234 [10.1039/c5sm00760g](https://doi.org/10.1039/c5sm00760g)